

Numerical simulation of bubble deformation and breakup under simple linear shear flows

Mitsuhiko Ohta^{a,b,*}, Tetsuya Ueta^b, Yozo Toei^c, Edwin Jimenez^d, Mark Sussman^e

^a*Department of Mechanical Science, Graduate School of Technology, Industrial and Social Sciences, Tokushima University, 2-1 Minamijyousanjima-cho, Tokushima 770-8506, Japan*

^b*Department of Mechanical Engineering, Graduate School of Technology, Industrial and Social Sciences, Tokushima University, 2-1 Minamijyousanjima-cho, Tokushima 770-8506, Japan*

^c*High Performance Plastics Company, Sekisui Chemical Co., Ltd., 2-1 Hyakuyama, Mishimagun Shimamoto-cho, Osaka 618-0021, Japan*

^d*Spectral Numerical, LLC, 1942 Broadway St., STE 314C, Boulder, CO 80302, USA*

^e*Department of Mathematics, Florida State University, Tallahassee, FL 32306, USA*

Abstract

Numerical simulations are presented for the deformation and breakup of a bubble in liquids undergoing simple linear shear flow. Numerical results are obtained using a hydrodynamic scheme with formal second-order accuracy based on a coupled level set/volume-of-fluid (CLSVOF) method. To verify our numerical algorithm and provide a basis for comparison, we also present simulation results that compare with previous, more popular, drop deformation and rupture simulations. The numerical results reveal that the shear-induced bubble deformation and breakup process differs significantly from that of the analogous drop system under similar flow conditions. The first distinguishing factor for bubble breakup is that the magnitude of shear flow necessary for causing rupture is much larger than that in the drop system case. In other words, a larger Reynolds number is needed to induce bubble breakup. The second distinct feature of the bubble system versus the drop system is that the bubble does not maintain a stable deformed shape as the system parameters approach the critical “breakup” Reynolds number. It is asserted that the differences in morphology for a bubble undergoing breakup versus a drop in the same process can be attributed to the density and viscosity ratio of the corresponding two-phase flow systems. The critical conditions for bubble breakup with respect to the Reynolds and capillary numbers are determined for several cases.

Keywords: Bubble deformation, bubble breakup, shear flow, CFD

*Corresponding author: m-ohta@tokushima-u.ac.jp

1 **1. Introduction**

2 Bubble dynamics in shear flow, including breakup, is critically important for
3 various gas-liquid scientific and engineering processes. We refer the reader to the
4 following experimental studies relating to bubble deformation in foaming pro-
5 cesses, microfluidic devices, and microbubbles in the blood circulation system,
6 [4, 23, 3, 8]. In particular, it is the study of bubble deformation as it pertains
7 to high-performance plastics applications that motivate this work. This article
8 presents computational studies of shear-driven deformation and breakup of a
9 bubble in insoluble viscous liquids. Studying bubble break-up via computation
10 rather than experiments simplifies the process of setting a combination of pre-
11 cise, simple shear flow conditions, low Ca conditions, low-density ratio, and low
12 viscosity ratios. The physical properties that distinguish bubble and drop stud-
13 ies are expressed in terms of the density ratio $\lambda = \rho_b/\rho_m$ and the viscosity ratio
14 $\eta = \mu_b/\mu_m$, where ρ is the fluid density, μ is the viscosity and the subscripts
15 “b” and “m” denote the “bubble” or “drop” and the “matrix fluid”, respec-
16 tively. For a bubble in an insoluble, viscous liquid, $\lambda \simeq 0$ and $\eta \simeq 0$, whereas
17 most studies dealing with a drop in an immiscible viscous liquid take $\lambda = 1$
18 and $\eta \simeq 1$. In this work, we focus on identifying critical flow states numeri-
19 cally, in terms of dimensionless quantities, that specify the extreme conditions
20 at which a bubble in shear flow first transitions from deformation to breakup.
21 We validate our numerical method by examining the sensitivity of the critical
22 bubble deformation and break-up flow states with respect to the grid size. An
23 advantage of studying shear-driven bubble deformation and breakup computa-
24 tionally rather than experimentally is that we can easily modify fluid physical
25 properties to ascertain the sensitivity of deformation and breakup to physical
26 parameters. In our computations, the time-evolution of the boundary between
27 gas and liquid is tracked with a coupled level set/volume-of-fluid (CLSVOF)
28 interface capturing algorithm [39, 41]. We focus on determining critical phys-
29 ical conditions in which the breakup of a bubble occurs in shear flow because
30 it is important to identify the parameter regimes in which a relatively simple
31 system transitions from stable to unstable. Specifically, we ascertain the critical
32 Reynolds number (Re_c) corresponding to the bubble breakup onset condition
33 as a function of Ca . In previous studies on the motion of bubble deformation
34 in a simple shear flow [35, 23], only findings for bubble deformation under very
35 low Re number conditions ($Re \ll 1$) have been reported. In this work, we de-
36 termine, for the first time, the critical Reynolds number ($Re \gg 1$) that leads to
37 bubble breakup. Additionally, our computational studies reveal characteristics
38 that distinguish a drop’s deformation and breakup processes versus those of a
39 bubble. We remark that there have been a number of articles on the study of
40 lift of slightly deformable bubbles[9, 21]. We reiterate, though, that for bubble
41 deformation and breakup in shear flows, only a few articles exist: [47, 46]. These
42 previous studies mainly examined the dynamics (e.g., rotation angle) of bubble
43 deformation in shear flow. Concerning bubble breakup, Wei et al. [47] presented
44 only one numerical result for a bubble breakup process under the condition of
45 Ca (capillary number) = 35.

46 To highlight the mechanisms of bubble deformation and breakup in a shear
47 flow, we juxtapose the bubble results with those of a drop. We remark that
48 while the study of critical tensile strength parameters for the bubble is sparse,
49 there have been many studies for the simpler drop problem. For completeness,
50 we give a brief overview of previous “tensile strength” studies pertaining
51 to drops. The study of the deformation and breakup of a drop in immiscible
52 viscous liquids undergoing simple linear shear flow has been investigated
53 extensively due to its fundamental importance to emulsion processes, materials
54 processing, mixing, and reaction devices. The pioneering experimental work
55 on this problem was performed by Taylor in the early 1930s [43, 44], and the
56 subsequent theoretical and experimental progress up to the 1980s and 1990s
57 was reviewed in [28] and [36], respectively. By the 2000s, progress in com-
58 putational fluid dynamics (CFD) techniques and increased access to powerful
59 computing resources led to a surge of research focused on direct simulations
60 of this problem. In particular, detailed computational investigations of drop
61 breakup, based on a Volume-of-Fluid (VOF) method [11] were presented in
62 [22, 32, 34, 33, 18, 29, 30, 31]. Since then, the literature on computational stud-
63 ies on the deformation and breakup of a single or several drops in shear flow
64 has continued to grow [6, 13, 48, 2, 15, 7, 19, 20, 14, 10, 1, 51] and a variety
65 of numerical techniques have been developed to tackle this problem, including
66 boundary-integral approaches [5, 16], lattice Boltzmann methods [12, 19], front
67 tracking schemes [45], and interface-capturing level set methods [40]. Thus, a
68 lot of studies about the deformation and breakup of a drop in simple linear
69 shear have been presented so far. In contrast, few studies have been conducted
70 on bubble deformation and breakup.

71 2. Problem Description

72 Figure 1(a) shows a schematic of the computational system for our studies
73 of a bubble (or drop) in shear flow. The computational domain consists of a
74 three-dimensional rectangular domain of L (length) \times W (width) \times H (height).
75 The size of L , W and H was determined after consideration of numerical result
76 sensitivity to domain size; numerical studies of domain-size dependence are
77 presented in Section 3.3. All computational results that follow were obtained
78 from numerical solutions of the three-dimensional governing equations for gas-
79 liquid/liquid-liquid flows. Computations are initialized with a spherical bubble
80 (or drop) of radius $R = 5$ mm set at the center of the computational domain.
81 The bubble (or drop) is then subjected to a linear shear flow generated by the
82 motion of the top and bottom plates, which have constant velocity $+V$ and
83 $-V$, respectively. In the interior of the domain, the initial velocity condition
84 is assumed to be a simple linear profile and periodic boundary conditions are
85 imposed along the x and y directions. Mathematically, the initial and boundary

86 conditions are described as follows:

$$\phi(x, y, z, 0) = \sqrt{(x - \frac{L}{2})^2 + (y - \frac{W}{2})^2 + (z - \frac{H}{2})^2 - R} \quad (1)$$

$$\mathbf{u}(x, y, z, 0) = \begin{pmatrix} \frac{2V}{H}(z - \frac{H}{2}) \\ 0 \\ 0 \end{pmatrix}$$

$$\phi(x + L, y, z, t) = \phi(x, y, z, t) \quad \phi(x, y + W, z, t) = \phi(x, y, z, t)$$

$$\mathbf{u}(x, y, H, t) = \begin{pmatrix} V \\ 0 \\ 0 \end{pmatrix} \quad \mathbf{u}(x, y, 0, t) = \begin{pmatrix} -V \\ 0 \\ 0 \end{pmatrix}$$

$$\mathbf{u}(x + L, y, z, t) = \mathbf{u}(x, y, z, t) \quad \mathbf{u}(x, y + W, z, t) = \mathbf{u}(x, y, z, t)$$

87 $\phi(x, y, z, t)$ is a material indicator function which is positive in the “matrix”
 88 fluid and negative in the bubble (or drop) fluid. $\mathbf{u}(x, y, z, t)$ is the velocity.

89 Common dimensionless physical parameters used to describe gas-liquid or
 90 liquid-liquid two-phase flows include the Reynolds (Re), Weber (We) (or Ca (=
 91 We/Re)) and Froude (Fr) numbers. Gas-Liquid and Liquid-Liquid two-phase
 92 flow problems are also determined by the density ratio λ and the viscosity ratio
 93 η . In the present study, in order to clearly isolate only the effects of λ and η ,
 94 the effect of gravity is not considered ($g = 0$) so that we ignore the effect of the
 95 Fr number $\left(= \frac{\Gamma R}{\sqrt{gR}}\right)$.

96 When comparing with previous drop studies, we fix $\lambda = 1$. As a result, (for
 97 $\lambda = 1$) the following dimensionless physical parameters are used to describe the
 98 problem of drop deformation/breakup in shear flow

$$Re = \frac{\rho_m U R}{\mu_m}, \quad Ca = \frac{\mu_m U}{\sigma}, \quad \eta = \frac{\mu_b}{\mu_m} \quad m = \text{matrix fluid} \quad (2)$$

99 U is the velocity scale and σ denotes the surface tension. For the problem of
 100 shear-induced drop deformation and breakup, the velocity is set to $U = \Gamma R$,
 101 where the shear-rate is $\Gamma = 2V/H$. As mentioned in the introduction, most
 102 previous drop studies set $\eta = 1$ (e.g. Li et al. [22]). Thus, for comparison
 103 with previous drop deformation and breakup problems, we set $\lambda = \eta = 1$ (and
 104 also neglect the effect of gravity so that $g = 0$). On the other hand, in our
 105 computations for bubble deformation, we set the density and viscosity of air to
 106 be $\rho_b = 1.2 \text{ kg/m}^3$ and $\mu_b = 1.8 \times 10^{-5} \text{ Pa}\cdot\text{s}$ respectively. We emphasize that for
 107 consistency with previous studies (Li et al. [22], Rust and Manga [35], Müller-
 108 Fischer et al. [23], Komrakova et al. [19], Amani et al. [1]), we computationally
 109 examine the deformation and breakup of a bubble in simple linear shear flow
 110 as a function of the Re and Ca numbers. That is to say, by setting $g = 0$,
 111 we are isolating the effect of only varying Re and Ca on bubble deformation
 112 and breakup. In our controlled study, we determine the critical Re_c versus Ca
 113 curve in which Re_c corresponds to the threshold of bubble (or drop) breakup.
 114 We determine the critical Re_c versus Ca curve for strategic pairs of the density
 115 ratio and viscosity ratio.

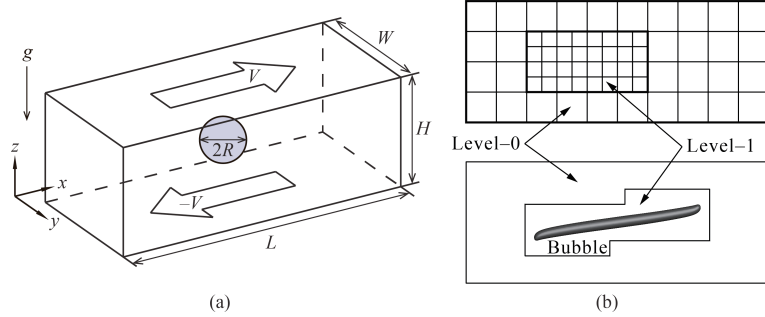


Figure 1: (a) Computational domain schematic for a bubble or drop in shear flow. Gravity is set to zero in our computations in order to isolate the effects of density and viscosity ratios. (b) (upper panel) a two-level adaptive mesh refinement (AMR) grid schematic corresponding to one of our simulations; (lower panel) snapshot of bubble deformation in simple linear shear flow.

116 In our computations, the density of the matrix fluid is fixed at $\rho_m = 1000$
 117 kg/m^3 . The surface tension at the bubble (drop) interface is $\sigma = 2.5 \times 10^{-2}$
 118 N/m . The values of Re and Ca in our simulations are controlled by changing
 119 the values of μ_m and V . Specifically, we set $\mu_m = 2.0 \times 10^{-2} \sim 6.0 \times 10^{-2}$
 120 $\text{Pa}\cdot\text{s}$ and $V = \text{about } 1.1 \sim 1.3 \text{ m/s}$. As a consequence, for studying bubble
 121 deformation and break-up, the density and viscosity ratios satisfy $\lambda = 1.2 \times 10^{-3}$
 122 and $\eta < 1.0 \times 10^{-3}$.

123 For readers' reference, we describe the effect of gravity here. When we apply
 124 $g = 9.8 \text{ m/s}^2$, Fr can be $Fr = 1.7 \sim 1.9$ in our computations. Although the
 125 values of Fr are not so large, the effect of gravity (bubble rise motion) may not
 126 be completely negligible in terms of Fr . However, bubbles in our computations
 127 reach the breakup by way of deformation very quickly at $t = \text{about } 0.5 \text{ s}$.
 128 Accordingly, it is expected that the effect of gravity (bubble rise motion) can
 129 be small for the behavior of bubble deformation and breakup around critical Re
 130 number conditions in our study.

131 3. Numerical Analysis

132 3.1. Numerical method and governing equations

133 Numerical results were obtained using the interface capturing Coupled Level
 134 Set and Volume of Fluid (CLSVOF) method (Sussman and Puckett [39], Suss-
 135 man et al. [41]), which is based on a fixed grid finite volume algorithm. The
 136 CLSVOF method is a robust numerical technique that combines some of the ad-
 137 vantages of the Volume of Fluid (VOF) method (Hirt and Nichols [11]) and the
 138 Level Set (LS) (Sussman et al. [40]) method while overcoming their weaknesses.
 139 In the VOF method, the Volume Fraction function, F , is used to represent
 140 the interface. The values of F correspond to the volume fraction of liquid in
 141 a given computational cell. In other words, $F = 0$ when a computational cell
 142 contains only gas and $F = 1$ when a computational cell contains only liquid.

143 If $0 < F < 1$, then a computational cell contains the gas-liquid interface. The
 144 VOF method has a great advantage over the LS method in that accurate algo-
 145 rithms for advecting F can be applied so that mass/volume is conserved up to
 146 machine precision while still maintaining a sharp representation of the interface.
 147 On the other hand, the disadvantage of the VOF method in comparison to the
 148 LS method is that tangled and difficult reconstruction procedures are required
 149 for determining the slope of the piecewise linear VOF reconstructed interface.
 150 In the LS method, the signed distance function ϕ (LS function) is used to track
 151 the interface. The interface is implicitly represented by the set of points in which
 152 $\phi = 0$. Liquid and gas regions are defined as $\phi > 0$ in the liquid and $\phi < 0$ in the
 153 gas, respectively. One of the advantages of the LS method is that one can track
 154 and represent smoothly the interface, but the LS method has the disadvantage
 155 that mass/volume is not explicitly conserved. In the CLSVOF method, the cou-
 156 pling between the LS function and the VOF function occurs when computing
 157 the normal of the reconstructed interface in the VOF calculation process and
 158 also when assigning the LS function with the exact signed normal distance to
 159 the reconstructed interface in the LS calculation process. That is to say, the
 160 piecewise linear approximation (the volume-of-fluid reconstruction step) for the
 161 VOF method is determined using the unit normal vector (\mathbf{n}) estimated from
 162 information of the LS function. By taking advantage of both methods, the evo-
 163 lution of the liquid-gas interface location can be computationally captured in
 164 such a way so that volume/mass is preserved to machine precision and at the
 165 same time, the interface normals and the surface tension force (which is pro-
 166 portional to the interface curvature) can be straightforwardly derived from the
 167 smooth level set function.

168 In our studies, the two-phase fluid flow is comprised of air and a viscous
 169 Newtonian liquid. The Heaviside function, $\mathcal{H}(\phi)$, which is defined as

$$\mathcal{H}(\phi) = \begin{cases} 1 & \phi \geq 0 \\ 0 & \phi < 0 \end{cases} \quad (3)$$

170 will be used below to distinguish each of the two fluids. A single set of three-
 171 dimensional equations governs the motion of both fluids, which are taken to be
 172 incompressible, and consists of the continuity equation and the Navier-Stokes
 173 equations with surface tension forces:

$$\nabla \cdot \mathbf{u} = 0 \quad (4)$$

$$\frac{\partial \mathbf{u}}{\partial t} + (\mathbf{u} \cdot \nabla) \mathbf{u} = \frac{1}{\rho} \nabla \cdot (-p \mathbf{I} + 2\mu \mathbf{D}) + \mathbf{g} - \frac{\sigma \kappa}{\rho} \nabla \mathcal{H} \quad (5)$$

174 where \mathbf{u} is the velocity vector, t represents time, p is the pressure, \mathbf{I} is the unit
 175 tensor, \mathbf{D} is the rate of deformation tensor ($\mathbf{D} = \frac{1}{2}(\nabla \mathbf{u} + (\nabla \mathbf{u})^T)$), ρ is the
 176 density, μ is the viscosity, κ is the interfacial curvature, and the Heaviside func-
 177 tion $\mathcal{H}(\phi)$ is a function of the level set (LS) function ϕ . The singular Heaviside
 178 gradient term in the right hand side of equation (5) is a body force representing
 179 the surface tension force and is equivalent to specifying that the jump in the

normal stress is equal to $\sigma\kappa$ (Tanguy et al. [42]). The surface tension force expressed by the singular Heaviside gradient term acts only on the gas-liquid interface. The sharp interface “Ghost Fluid Method” (Kang et al. [17]) is used to discretize the gradient of the Heaviside function as it appears in the surface tension force term. This force, upon discretization, is only non-zero across cells in which the level set function changes sign.

The interfacial curvature κ is computed with second order accuracy directly from the volume-of-fluid (VOF) function using the height function technique (Sussman [37], Sussman et al. [41]). We remark that we get the same results if we were to compute κ directly from the LS function using the “level set” height function technique.

Since ρ and μ are taken to be constant in each fluid, with a jump at the interface, they can be expressed in terms of the Heaviside function,

$$\rho = \rho_m \mathcal{H} + \rho_b (1 - \mathcal{H}), \quad \mu = \mu_m \mathcal{H} + \mu_b (1 - \mathcal{H}). \quad (6)$$

The subscripts “b” and “m” refer to “drop or bubble” and “matrix fluid”, respectively. To represent the free surface with the CLSVOF method, we must evolve the solution to both the VOF equation for F and the LS equation for ϕ :

$$\frac{\partial F}{\partial t} + (\mathbf{u} \cdot \nabla) F = 0, \quad \frac{\partial \phi}{\partial t} + (\mathbf{u} \cdot \nabla) \phi = 0. \quad (7)$$

In all computations the discretized variables p , ϕ and F are located at cell centers and the discrete variable \mathbf{u} is located at cell face centers. Our computations are performed using an overall second-order accurate hydrodynamic scheme. The spatial discretization uses second-order accurate, slope-limited, upwind techniques for the nonlinear advective terms. The velocity and pressure fields are computed using an implicit pressure projection procedure.

The temporal discretization of our numerical method is an operator split projection method as described by Sussman et al. [41]. An outline of our method is as follows (see Sussman et al. [41], section 4, for more details):

Timestep Δt The timestep is governed by the CFL condition and surface tension (section 5.7 of Sussman et al. [41]):

$$\Delta t < \min_{i,j,k} \left(\frac{\Delta x}{2|U^n|}, \frac{1}{2} \sqrt{\frac{\rho^L}{8\pi\sigma}} \Delta x^{3/2} \right)$$

Step 1. CLSVOF interface advection

$$\begin{aligned} \phi^{n+1} &= \phi^n - \Delta t [\mathbf{u} \cdot \nabla \phi]^n \\ F^{n+1} &= F^n - \Delta t [\mathbf{u} \cdot \nabla F]^n \end{aligned}$$

Step 2. Nonlinear advective force terms

$$\mathcal{A} = [\mathbf{u} \cdot \nabla \mathbf{u}]^n$$

Step 3. Viscosity force

$$\frac{\mathbf{u}^* - \mathbf{u}^n}{\Delta t} = -\mathcal{A} + g\vec{z} - [\nabla p/\rho]^n + \frac{1}{2} \frac{\nabla \cdot (2\mu \mathbf{D}^n) + \nabla \cdot (2\mu \mathbf{D}^*)}{\rho}$$

207 Step 4. Pressure projection and ghost fluid surface tension algorithm

$$\mathbf{V} = \mathbf{u}^n + \Delta t(-\mathcal{A} + g\vec{z} + \frac{1}{2} \frac{\nabla \cdot (2\mu \mathbf{D}^n) + \nabla \cdot (2\mu \mathbf{D}^*)}{\rho})$$

208

$$\mathbf{V} = \mathbf{V} - \Delta t \frac{\sigma \kappa(\phi^{n+1})}{\rho} \nabla \mathcal{H}(\phi^{n+1})$$

209

$$\nabla \cdot \frac{\nabla p}{\rho} = \frac{1}{\Delta t} \nabla \cdot \mathbf{V}$$

210

$$\mathbf{u}^{n+1} = \mathbf{V} - \Delta t \frac{\nabla p}{\rho}$$

211 To make efficient use of computational resources, our numerical simulations
 212 utilize an adaptive hierarchy of grids based on a dynamic adaptive mesh refine-
 213 ment (AMR) technique (Sussman et al. [38]). Adaptive grids are dynamically
 214 adjusted based on the location of the deforming gas-liquid interface. In the AMR
 215 technique the grid resolution is increased in regions near the interface while a
 216 coarser grid is used where the flow is relatively steady. The upper panel of
 217 Figure 1(b) displays a schematic view of the hierarchical grid structure and the
 218 lower panel corresponds to an actual computational example for bubble defor-
 219 mation in simple linear shear flow. In general, the mesh hierarchy is composed
 220 of different levels of refinement ranging from coarsest $\ell = 0$ (“level-0”) to finest
 221 $\ell = \ell_{\max}$ (“level- ℓ_{\max} ”). The refinement ratio of one grid size ($\Delta x = \Delta y = \Delta z$)
 222 to the next finer level is two so that $\Delta x^{\ell+1} = 0.5\Delta x^\ell$. All computations in
 223 this study used an AMR system with a maximum prescribed level $\ell_{\max} = 1$
 224 (as illustrated in the upper panel of Figure 1(b)). In our adaptive mesh refine-
 225 ment algorithm, the velocity in coarse grid cells that neighbor fine grid cells is
 226 interpolated from the coarse grid using bilinear interpolation in order to ini-
 227 tialize “ghost” fine cells. Thus, the bilinear interpolation procedure produces
 228 interpolated fine grid data as a linear combination of the coarse grid data.

229 *3.2. Validation of the numerical method*

230 The effectiveness of our computational method has been demonstrated for
 231 the complicated rising motion of single bubbles and drops in viscous liquids
 232 Ohta and Sussman [27], Ohta et al. [24, 25]. In this section, the accuracy
 233 of our computational method will be verified for the problem of shear-induced
 234 deformation of a drop and bubble. First, we compare quantitatively against

235 the steady-state drop deformation results reported by Li et al. [22]. The shape
 236 of a deformed drop in simple linear shear flow is described in terms of the Taylor
 237 deformation parameter $D = (a - b)/(a + b)$, where a and b are the major and minor
 238 axes of the deformed drop. For consistency, we perform numerical simulations
 239 using CLSVOF over the same computational domain and grid size used in Li
 240 et al. [22], which has dimensions $L(8R) \times W(4R) \times H(8R)$ (recall that R is the
 241 bubble/drop radius) and a level-0 grid size $\Delta x = \Delta y = \Delta z = R/8$; our two-level
 242 AMR grid structure also uses a finer level-1 grid size $\Delta x^{\ell=1} = \Delta y^{\ell=1} = \Delta z^{\ell=1} =$
 243 $R/16$. Numerical results are listed in Table 1 for D as a function of Re , with
 244 $Ca = 0.3$ and $\lambda = \eta = 1$ fixed in every case, obtained with the VOF method
 245 used in Li et al. [22], and also with our CLSVOF algorithm. Table 1 indicates
 246 that our numerical results are in good agreement with previous computations
 for drop deformation and breakup.

Table 1: Comparison of the Taylor deformation parameter D for a drop as a function of Re ($Ca = 0.3$, $\lambda = \eta = 1$). In all cases, the domain size is $L(8R) \times W(4R) \times H(8R)$, where R is the drop radius. CLSVOF method computations used a two-level AMR computational domain with a level-0 discretization $\Delta x^{\ell=0} = \Delta y^{\ell=0} = \Delta z^{\ell=0} = R/8$ and a level-1 discretization $\Delta x^{\ell=1} = \Delta y^{\ell=1} = \Delta z^{\ell=1} = R/16$.

Reynolds number	0.1	0.5	0.6	0.75
D (Li et al. [22])	0.3968	0.45	0.4768	Breakup
D (Our study)	0.3960	0.4570	0.4758	Breakup

247 Next, we examine the validation of our computational method in which we
 248 compare with the “bubble deformation in simple linear shear flow” results re-
 249 ported by Müller-Fischer et al. [23]. Müller-Fischer et al. [23] experimentally
 250 inquired into the bubble deformation under the condition of $Re \approx 0$. In our
 251 study, we computed the bubble deformation on a computational domain with
 252 dimensions $L(12R) \times W(6R) \times H(6R)$ and a computational grid in which the
 253 finest level grid size was $\Delta x^{\ell=1} = \Delta y^{\ell=1} = \Delta z^{\ell=1} = R/16$. Computations
 254 were performed for the conditions of $Ca = 0.96$ and $Ca = 1.63$ with $Re \approx 0$
 255 ($Re = 5.0 \times 10^{-4}$), $\lambda = 1.2 \times 10^{-3}$ and $\eta \leq 1.2 \times 10^{-6}$. The parameters
 256 that we have prescribed are consistent with the experimental conditions by
 257 Müller-Fischer et al. [23]. Comparisons of our numerical results and previous
 258 experimental results (Müller-Fischer et al. [23]) are tabulated in Table 2. Ad-
 259 ditionally, in Table 2, we also list experimental results with the condition of
 260 $Re \approx 0$ and $\lambda \approx \eta \approx 0$ by Rust and Manga [35]. These experimental values
 261 were obtained from the graph showing the relation of D vs Re (Rust and Manga
 262 [35]). As is clear from Table 2, our numerical results predicted larger values of
 263 D than experimental ones reported by Müller-Fischer et al. [23]. Nevertheless,
 264 we found that our numerical results are very close to the experimental results
 265 by Rust and Manga [35], which emphasizes the intrinsic difficulties associated
 266 with experimental investigations of bubble dynamics, even in simple linear shear
 267 flow. These comparisons suggest that our computational method is effective and
 268 robust at reproducing bubble dynamics in simple linear shear flow.

Table 2: Comparison of D for a bubble as a function of Ca ($Re \approx 0$, $\lambda \approx \eta \approx 0$). In all cases, the domain size is $L(12R) \times W(6R) \times H(6R)$. CLSVOF computations used a two-level AMR computational domain with a level-0 discretization $\Delta x^{\ell=0} = \Delta y^{\ell=0} = \Delta z^{\ell=0} = R/8$ and a level-1 discretization $\Delta x^{\ell=1} = \Delta y^{\ell=1} = \Delta z^{\ell=1} = R/16$.

Capillary number	0.96	1.63
D (Müller-Fischer et al. [23])	0.37	0.58
D (Rust and Manga [35])	0.71 ± 0.05	0.81 ± 0.02
D (Our study $\Delta x^{\ell=1} = R/16$)	0.63	0.71

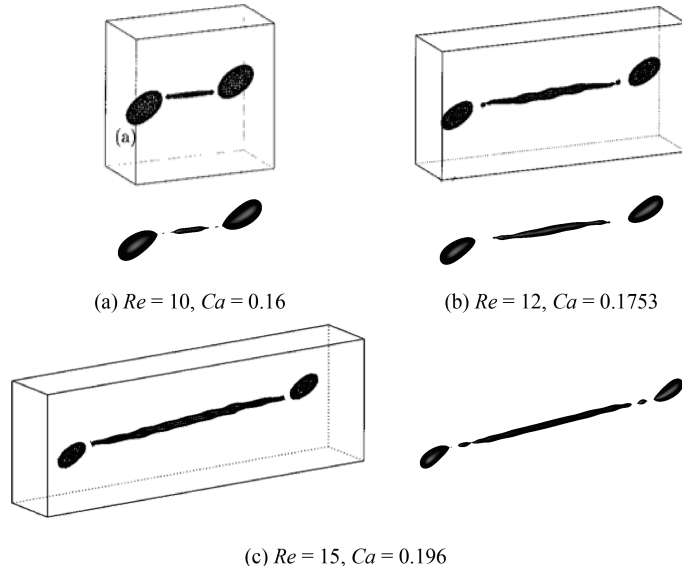


Figure 2: Comparison with results reported in Renardy and Cristini [34] (shown in boxes) for drop breakup in shear flow. In Renardy and Cristini [34], the computational domain dimensions were $W = 4R$, $H = 8R$, and L was varied depending on the Re and Ca conditions. The grid size in Renardy and Cristini [34] was set to $\Delta x = \Delta y = \Delta z = R/8$. Reprinted with permission from reference Renardy and Cristini [34]. Copyright 2001, AIP Publishing. Results obtained with our CLSVOF algorithm, corresponding to each case in reference Renardy and Cristini [34], are shown outside boxes. The CLSVOF method used a two-level AMR computational domain with a level-0 discretization $\Delta x^{\ell=0} = \Delta y^{\ell=0} = \Delta z^{\ell=0} = R/8$ and a level-1 discretization $\Delta x^{\ell=1} = \Delta y^{\ell=1} = \Delta z^{\ell=1} = R/16$. The onset of drop breakup is demonstrated for (a) $Re = 10$, $Ca = 0.16$, (b) $Re = 12$, $Ca = 0.1753$, and (c) $Re = 15$, $Ca = 0.196$. For all three Re and Ca conditions, $\lambda = \eta = 1$.

Finally, we present a comparison with numerical results for drop breakup reported in Renardy and Cristini [34]. Figure 2 demonstrates drop breakup with pinch-off behavior for three Re and Ca conditions and with constant values of $\lambda = \eta = 1$ for all cases. The three cases that we consider correspond to (a) $Re = 10$, $Ca = 0.16$, (b) $Re = 12$, $Ca = 0.1753$, and (c) $Re = 15$, $Ca = 0.196$, and which are illustrated in Figures 2(a)-(c), respectively. The results

276 reported in Renardy and Cristini [34], which were obtained with a VOF method,
 277 are shown inside boxes while results obtained with our CLSVOF approach are
 278 displayed outside boxes. In the computations presented in Renardy and Cristini
 279 [34], the dimensions $W = 4R$ and $H = 8R$ were fixed, while L was changed
 280 depending on Re and Ca conditions, and the grid size was set to $\Delta x = \Delta y =$
 281 $\Delta z = R/8$. To compare with their results, we performed simulations with the
 282 CLSVOF method over a two-level AMR computational domain of the same
 283 dimensions and the same level-0 discretization: $\Delta x^{\ell=0} = \Delta y^{\ell=0} = \Delta z^{\ell=0} =$
 284 $R/8$; we set the finer level-1 grid size $\Delta x^{\ell=1} = \Delta y^{\ell=1} = \Delta z^{\ell=1} = R/16$. The
 285 results shown in Figure 2 verify that our numerical approach can reproduce
 286 the same drop breakup behavior presented in Renardy and Cristini [34]. Slight
 287 differences between the results can be attributed to the increased resolution used
 288 in our study in the level-1 grid around the elongated drop.

289 The numerical validation studies performed in this section and the follow-
 290 ing section demonstrate that our numerical method can reliably determine the
 291 transition regions at which shear-induced bubble or drop deformation leads to
 292 breakup. We remark that in the next section, we demonstrate that we can
 293 expect an error of 3% for predicting the transition to break-up. The analysis
 294 in this section and the following also demonstrate that the error is reduced by
 295 a factor of 2 each time the grid is refined by a factor of 2. Also, we refer the
 296 reader to Ohta et al. [26] in which we apply our CLSVOF method for bubble
 297 formation problems.

298 3.3. Consideration of domain and grid sizes

299 3.3.1. Selecting the appropriate domain size

300 The computational domain size used in numerical studies can affect the
 301 behavior of drop deformation and breakup. Referring to Figure 1(a), with an
 302 appropriately large domain length L and a fixed width $W = 4R$, the effect of
 303 the height H on drop behavior was examined in Li et al. [22] for Stokes flows
 304 and various Ca conditions and in Komrakova et al. [19] for $Re = 1$ and $Ca =$
 305 0.27. Other related studies investigated drop breakup sensitivity (Renardy and
 306 Cristini [32]) and drop deformation sensitivity (Renardy et al. [33]) with respect
 307 to the entire domain size.

308 Here we investigate the drop dynamics sensitivity to domain size around
 309 the critical Reynolds number $Re_c = 0.75$. Specifically, we consider domain size
 310 sensitivity for the condition of $Re = 0.75$, $Ca = 0.3$, and $\lambda = \eta = 1$, which is a
 311 condition used in the comparison studies of the previous section. As shown in
 312 Table 1, the drop breaks up for the condition of $Re = 0.75$ and $Ca = 0.3$ with
 313 a domain size of $L(8R) \times W(4R) \times H(8R)$. Results for domain size sensitivity
 314 for six domain systems, all of which use a level-1 grid size $\Delta x^{\ell=1} = \Delta y^{\ell=1} =$
 315 $\Delta z^{\ell=1} = R/16$, are tabulated in Table 3. Note that the domain size used in the
 316 comparison study (Table 1) corresponds to System 1.

317 The results in Table 3 suggest that drop deformation is promoted when we
 318 use a domain size with $W = 4R$. In contrast, the drop does not break up and
 319 becomes stable with a deformed shape if we set L large enough and $W \geq 6R$ and

Table 3: Comparison of the Taylor deformation parameter D for a drop as a function of domain size ($Re = 0.75$, $Ca = 0.3$, $\lambda = \eta = 1$). CLSVOF method computations used a two-level AMR computational domain with a level-0 discretization $\Delta x^{\ell=0} = \Delta y^{\ell=0} = \Delta z^{\ell=0} = R/8$ and a level-1 discretization $\Delta x^{\ell=1} = \Delta y^{\ell=1} = \Delta z^{\ell=1} = R/16$.

System	Domain size ($L \times W \times H$)	D
System 1	$8R \times 4R \times 8R$	Breakup
System 2	$12R \times 4R \times 8R$	Breakup
System 3	$8R \times 4R \times 6R$	0.541
System 4	$8R \times 6R \times 6R$	0.466
System 5	$8R \times 8R \times 8R$	0.460
System 6	$8R \times 16R \times 16R$	0.460

320 $H \geq 6R$. Since the value of D for the domain size $L(8R) \times W(6R) \times H(6R)$ differs
321 by only 1.3% with the value for the domain size of $L(8R) \times W(16R) \times H(16R)$,
322 in the results that follow we set the width to $W = 6R$ and the height to $H = 6R$
323 to minimize the number of computational grid nodes along those directions. To
324 determine the critical Reynolds number Re_c (with $Ca = 0.3$), we consider a
325 domain size of $L(24R) \times W(6R) \times H(6R)$, and we find that the drop reaches a
326 stable state with deformation parameter $D=0.549$ for $Re = 1.0$, while a value
327 of $Re = 1.1$ leads to drop breakup.

328 *3.3.2. Selecting the appropriate grid size*

329 The grid size and adaptive meshing strategy that we adopt is chosen in order
330 to answer the research question as to the conditions which determine whether
331 a bubble in shear flow will break-up or not. In such a case, we must accurately
332 capture the balance of forces with respect to the (non-local) force exerted from
333 the wall driven flow acting against the interfacial surface tension force. The
334 accuracy of the “Critical Reynolds Number” depends on the largest Taylor De-
335formation parameter D that is supported by the grid (see e.g. Figures 8 and
336 11). As we report here, we have found that as long as the grid size is fine enough
337 to support a Taylor Deformation parameter $D < 0.95$, then the transition re-
338gion (i.e. “Critical Reynolds number”) (see Figures 3 and 12) will be captured
339 with a tolerance of three percent. The simulation time becomes impractical if
340 we were to try to further improve the “critical Reynolds number” accuracy. A
341 smaller tolerance would necessitate a larger supported Deformation parameter
342 D which would in turn necessitate a higher aspect ratio computational domain,
343 increased droplet surface area at break-up, increased number of time steps, and
344 higher resolution for representing the drop/bubble at its thinnest point.

345 We make the distinction between our present research, and the research
346 found in the work of Zhang et al. [49, 50] on predicting the conditions for bubble
347 mergers. Even in the most extreme cases for mergers, the largest Deformation
348 parameter never exceeds 0.4 in Zhang et al. [49]. In summary, our gridding
349 requirements necessitate grid points distributed relatively evenly throughout the
350 computational domain when a bubble is stretched to a $D = 0.9$ Deformation,

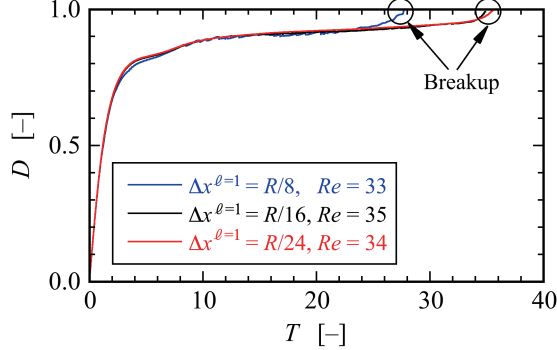


Figure 3: Time evolution of the deformation parameter D versus dimensionless time $T = \Gamma t$ for a bubble, obtained with three grid systems at different resolutions. All three resolutions use a two-level AMR grid with an effective fine resolution grid size $\Delta x^{\ell=1} = \Delta y^{\ell=1} = \Delta z^{\ell=1}$. The evolution of D using the first system, where $\Delta x^{\ell=1} = R/8$, is shown in blue and it predicts that bubble breakup occurs at a Reynolds number $Re = 33$. The evolution of D using the second system, where $\Delta x^{\ell=1} = R/16$, is shown in black and it predicts that bubble breakup occurs at a Reynolds number $Re = 35$. Results with the third system, shown in red, use $\Delta x^{\ell=1} = R/24$, and they predict that breakup occurs at $Re = 34$. The capillary number corresponding to these results is $Ca = 1.0$. ($\lambda = 1.2 \times 10^{-3}$, $\eta < 1.0 \times 10^{-3}$)

whereas in Zhang et al. [49] the gridding strategy necessitates a more localized strategy.

The numerical results presented in this and the previous section used a finest-level grid size set to $\Delta x^{\ell=1} (= \Delta y^{\ell=1} = \Delta z^{\ell=1}) = R/16$. To verify the adequacy of this grid resolution, we present grid refinement results for a bubble breakup simulation with $Ca = 1.0$, which corresponds to the most deformable and stretchable bubble case considered in our numerical studies. We use three different grid systems, (i) $\Delta x^{\ell=1} = R/8$, (ii) $\Delta x^{\ell=1} = R/16$, and (iii) $\Delta x^{\ell=1} = R/24$, in order to determine Re_c . Figure 3 shows the time evolution of the deformation parameter D over time for the three grid systems; the x -axis is a dimensionless time defined by $T = \Gamma t$ and the y -axis is D . The results show that bubble breakup occurs at $Re_c = 35$ for the grid system with $\Delta x^{\ell=1} = R/16$, while the finer computational grid with $\Delta x^{\ell=1} = R/24$ predicts a critical value of $Re_c = 34$. For the $\Delta x^{\ell=1} = R/8$ results, it is clear that the $R/8$ resolution is too coarse in order to capture the proper break-up time, albeit the critical Reynolds' number, $Re_c = 33$, was still close to the finer grid resolution cases. Note that although the time evolution of D for the two finer resolution systems ($R/16$ and $R/24$) is consistent between the two, (the predicted critical Reynolds numbers differ by $\sim 3\%$), the computational time using the grid system with $\Delta x^{\ell=1} = R/24$ was more than 6 times longer than the one based on the coarser system with $\Delta x^{\ell=1} = R/16$. We remark that in our search for Re_c , we considered a wide range of values of Ca and we found it necessary to use a large L ($\sim 24R$) since for certain shear flows the bubble can stretch significantly without breaking up. Nevertheless, for the conditions presented in this section, the results indicate

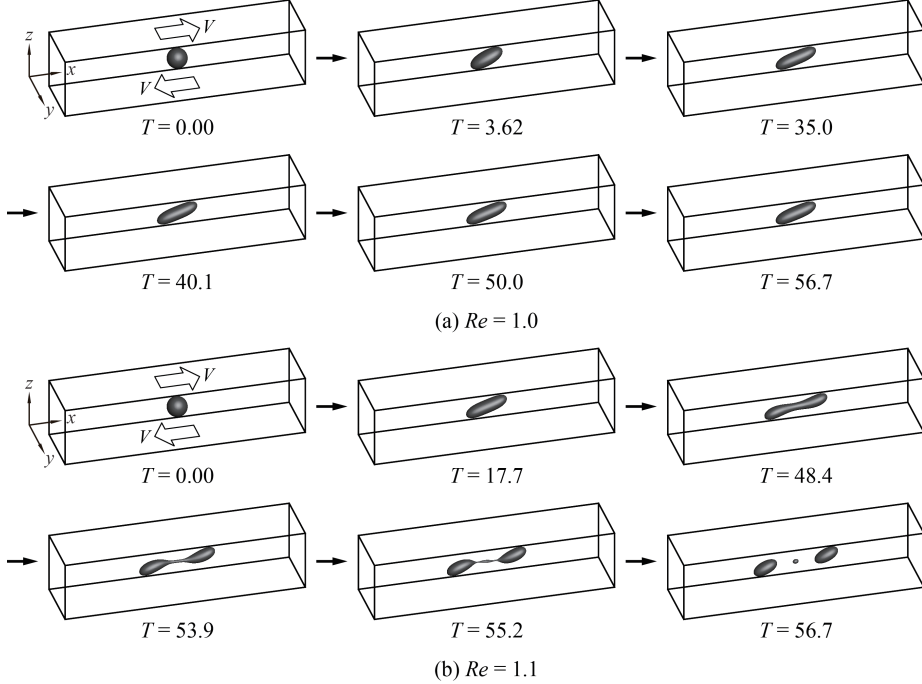


Figure 4: Time evolution of drop deformation and breakup in shear flow at the condition of $Ca = 0.3$ with (a) $Re = 1.0$ and (b) $Re = 1.1$. The “drop” critical Reynolds number corresponding to $Ca = 0.3$ is $1.0 < Re_c < 1.1$. ($\lambda = \eta = 1.0$)

375 that our numerical approach, even with a finest-level resolution set to $\Delta x^{\ell=1} =$
 376 $R/16$, is capable of accurately reproducing bubble deformation and breakup
 377 without sacrificing any essential dynamical features.

378 4. Results and Discussion

379 4.1. Drop deformation and breakup

380 To illustrate the differences in deformation and breakup between a drop
 381 and a bubble around critical conditions, we first present numerical results for
 382 drop deformation. The time evolution of drop deformation and breakup in
 383 simple linear shear flow for two conditions is shown in Figure 4; the first case,
 384 shown in Figure 4(a), uses $Ca = 0.3$ and $Re = 1.0$, while the second case,
 385 depicted in Figure 4(b), uses $Ca = 0.3$ and $Re = 1.1$. Using a domain size of
 386 $L(24R) \times W(6R) \times H(6R)$, in the case with $Re = 1.0$, the drop gradually deforms
 387 and finally attains a stable deformed state. After $T = 35.0$, the drop remains a
 388 **stable deformed state with $D = 0.549$** . Over the same domain, for the case with
 389 $Re = 1.1$, the “mother” drop elongates over time and the volume at the ends
 390 of the deforming drop expands; that is, both ends of the drop become bulb-
 391 shaped. As time progresses, particularly over the time interval $48.4 \leq T \leq 55.2$,

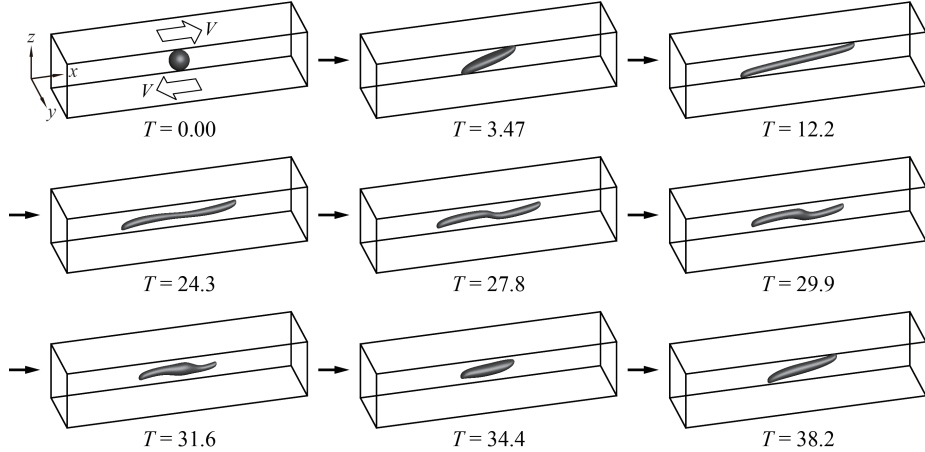


Figure 5: Time evolution of bubble deformation in shear flow at the condition of $Ca = 0.3$ and $Re = 92$. The “bubble” critical Reynolds number corresponding to $Ca = 0.3$ is $92 < Re_c < 93$. In contrast to the drop deformation case, when Re is slightly below Re_c (See Figure 4.1 $Re = 1.0$ for the drop case), the bubble shape will not reach a steady shape, instead the bubble shape alternates between the shapes “slightly stretched” ($T = 3.47$), fully stretched and “doglegged” ($T = 27.8$) and “almost” back to the original “slightly stretched” case ($T = 34.4$). ($\lambda = 1.2 \times 10^{-3}$, $\eta < 1.0 \times 10^{-3}$)

392 a thread-bridge forms between the bulbous ends and the thread-bridge becomes
 393 thinner. Finally, at around the dimensionless time $T \sim 56.7$, the mother drop
 394 breaks up, forming two “daughter” drops through the pinch off; one satellite
 395 drop is also generated between the pinched off daughter drops.

396 4.2. Bubble deformation and breakup

397 Next we present numerical results that illustrate the conditions that lead
 398 to bubble deformation without breakup as well as conditions where the bubble
 399 deforms and ultimately breaks up. The time evolution of shear-induced bubble
 400 deformation without breakup at the condition of $Ca = 0.3$ and $Re = 92$ is
 401 depicted in Figure 5 and the bubble breakup process with flow condition of
 402 $Ca = 0.3$ and $Re = 93$ is illustrated in Figure 6. The results indicate that
 403 the critical Reynolds number is approximately $Re_c = 93$ (with $Ca = 0.3$).
 404 A comparison with the drop breakup dynamics presented in Section 4.1 and
 405 the corresponding processes for bubble deformation and breakup exhibit very
 406 distinct features. First, we note that a relatively large shear force magnitude is
 407 required for bubble breakup ($\lambda = 1.2 \times 10^{-3}$, $\eta < 1.0 \times 10^{-3}$) compared with the
 408 case of the drop ($\lambda = \eta = 1$). Then, for the same value of $Ca = 0.3$, the critical
 409 Reynolds number for the bubble is around 85 times larger than that for the
 410 drop. Focusing on the bubble dynamics with no-breakup (Figure 5), the results
 411 show that the bubble is largely elongated in the x -direction at the early stages
 412 ($T \leq 24.3$) of bubble deformation, but the bubble does not develop the bulb-
 413 like shape (large volume areas) at both ends present in the drop deformation

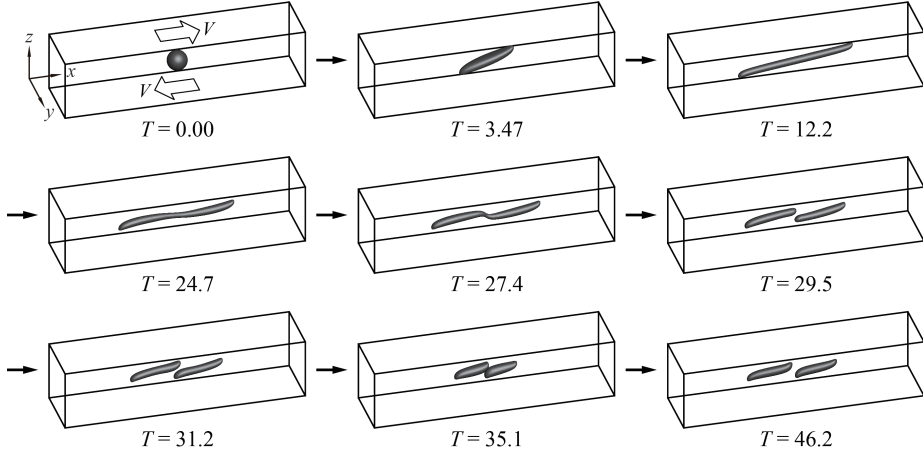


Figure 6: Time evolution of bubble deformation in shear flow at the condition of $Ca = 0.3$ and $Re = 93$. The “bubble” critical Reynolds number corresponding to $Ca = 0.3$ is $92 < Re_c < 93$. ($\lambda = 1.2 \times 10^{-3}$, $\eta < 1.0 \times 10^{-3}$)

process. It is also evident that the ends of the deforming bubble develop cusped shapes under the influence of the strong shear flow. In providing a more detailed description, very large shear forces are required to deform the bubble because $\lambda \simeq 0$ and $\eta \simeq 0$. Thus, the bubble undergoing large shear forces at $T > 0$ is largely stretched long the shear flow direction, and the very long elongated bubble with cusped shapes is formed. Accordingly, the bubble finally breaks up through f the elongated shape without forming a bulb-like shape. A noteworthy feature for the non-breaking bubble is that it does not settle into a deformed stable state as in the case of drop deformation presented in Figure 4.1(a). After an initial elongation process, the bubble enters a shrinking phase ($T = 27.8$) where the doglegged shape formed at the center of the bubble returns to a smaller deformed shape ($T = 34.4$) that is similar to its earlier shape ($T = 3.47$). However, when we compare the early deformed bubble shape at $T = 3.47$ with the shape at $T = 34.4$, it is clear that the shapes are not identical. Following the shrinking phase, the bubble begins to stretch again ($T = 38.2$) and the bubble oscillates between its elongated shape and shortened geometry.

For the case of bubble breakup (Figure 6), we observe that the deformation process is almost the same as the no-breakup case until the doglegged shape is formed at $T \sim 27.4$. The bubble finally breaks during the time interval $27.7 \leq T \leq 29.5$. For a closer examination of the bubble breakup process, a detailed panel of cross-sectional slices in the xz -plane through the bubble shape center is presented in Figure 7. The images displayed in Figure 7, which are taken at shorter time intervals than those shown in Fig. 6, reveal that the bubble breaks up into two daughter bubbles due to the pinch off at the thread-bridge part of the doglegged shape during the shrinking process ($T = 28.5 \sim 28.8$). After breaking up, the two daughter bubbles migrate to the center: the

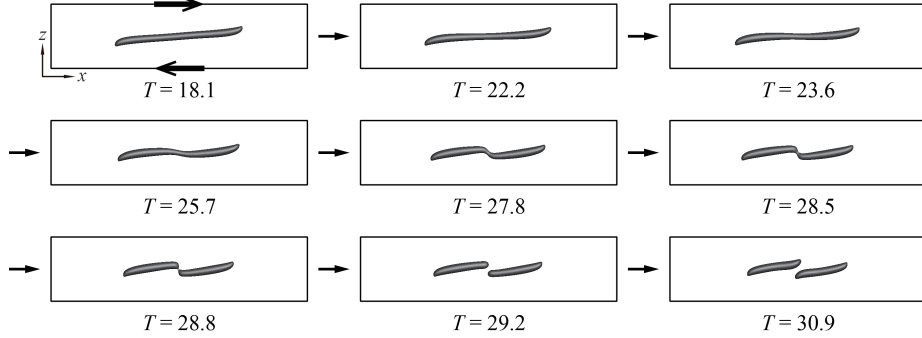


Figure 7: Detail of bubble breakup process in shear flow at the condition of $Ca = 0.3$ and $Re = 93$. The “bubble” critical Reynolds number corresponding to $Ca = 0.3$ is $92 < Re_c < 93$. ($\lambda = 1.2 \times 10^{-3}$, $\eta < 1.0 \times 10^{-3}$)

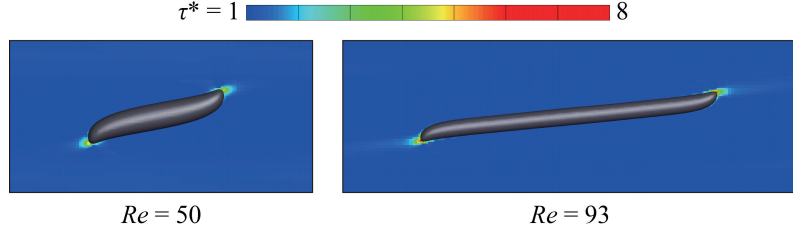


Figure 8: Normalized shear stress τ^* around a bubble for two Reynolds numbers under the condition of $Ca = 0.3$. The left image shows the shear stress profile at $Re = 50$ and the right image at $Re = 93$.

left daughter bubble moves toward the right-side of the domain and the right daughter bubble moves to the left side (see results for $T = 29.5 \sim 35.1$ in Figure 6 and for $T = 28.8 \sim 30.9$ in Figure 7). The two daughter bubbles then momentarily congregate near the domain center ($T = 35.1$ in Figure 6), before they slowly start to separate: the left daughter bubble moves to the left and the right daughter bubble moves to the right ($T = 46.2$ in Figure 6). The results clearly demonstrate that the bubble breakup process is markedly different from the analogous drop breakup process with $\lambda = 1$ and $\eta = 1$. Note that the appearance of deformation and breakup of the drop will largely depend on the viscosity ratios.

4.3. Shear stress acting on the bubble

In the previous section, the appearance of bubble deformation and breakup was discussed. It is expected that a large deformation and breakup of the bubble are closely related to the state of shear stress acting on the bubble. Figure 8 shows the shear stress profile around a bubble for two Reynolds numbers under the condition of $Ca = 0.3$: Reynolds number equal to 50 and 93. The shear stress profile on the left corresponds to the case of $Re = 50$ and the right side

457 shows the shear stress profile for the case of $Re = 93$. The normalized shear
 458 stress, $\tau^* = \tau/\tau_0$, is defined as a ratio of the local shear stress $\tau = \mu_m \sqrt{2\mathbf{D} : \mathbf{D}}$
 459 and the apparent shear stress $\tau_0 = \mu_m \Gamma$. In this study, for a given Ca condition,
 460 the same value of τ_0 is used regardless of Re . For the case of $Re = 50$, the bubble
 461 reached a deformed stable state, **and the shear stress profile around the bubble**
 462 **was drawn after the bubble attained a stable deformed state.** As observed
 463 in previous sections, when the value of Re is slightly below the critical Re
 464 condition, the bubble does not settle into a deformed stable state but instead
 465 alternates in an elongation and contraction process. **The shear stress profile for**
 466 **the case of $Re = 93$ was depicted when the bubble sufficiently elongated ($T =$**
 467 **14.9).** In comparison to the $Re = 50$ case on the left, the right image in Fig. 8
 468 ($Re = 93$) shows a higher shear stress profile near the bubble endpoints as it
 469 undergoes an elongation state in the process toward breakup. The value of the
 470 maximum shear stress for the case of $Re = 50$ is $\tau^* \approx 6$ and the maximum shear
 471 stress for the case of $Re = 93$ at the moment shown in Fig. 8 has the value of
 472 $\tau^* \approx 8$. The shear stress profile in Fig. 8 (color contour) is drawn in the range
 473 from $\tau^* = 1$ to $\tau^* = 8$, but, for emphasis, shear stress regions with $\tau^* \geq 6$ are
 474 illustrated in red. As can be seen in the figure, the strongest shear stresses are
 475 concentrated on the ends of the bubble for both Re conditions. This indicates
 476 that the strong shear stresses acting on the ends of the bubble are responsible
 477 for much of the bubble stretching. It is important to note that the magnitude
 478 of the shear stress acting on the ends of the bubble for the case of $Re = 93$ is
 479 much larger than that for the case of $Re = 50$.

480 We also observe that the shear stress inside the bubble was very small relative
 481 to that of the matrix fluid due to very small density and viscosity of the bubble.
 482 Since the force of strong shear stresses acting on the ends of the bubble is
 483 difficult to transfer across the interface, as a consequence, a sufficiently large Re
 484 condition is required for large bubble deformations.

485 In summary, what we discover is that for the Reynolds number sufficiently below
 486 the critical value, a relatively quick unsteady elongation period gives way to a
 487 steady state (with no break up). On the other hand for Reynolds number close
 488 to the critical Reynolds number, there is a prolonged, unsteady, elongation
 489 period, in which periodic motion is observed and the deformation parameter
 490 D is close to one. The “vacillating” behavior cannot last forever, ultimately
 491 (perhaps stochastically!), the bubble will either settle down or break. We assert
 492 that regardless of the outcome, this vacillating behaviour will always occur in
 493 close proximity to the critical Reynolds’ number. In other words, regardless of
 494 the outcome, we claim, using the grid resolution of $R/16$, that one is assured
 495 of being within 3 percent of the critical Reynolds number (see Figure 3). In
 496 fact, we hypothesize that there will always be “vacillating” behavior if one is
 497 sufficiently close to the critical Reynolds number. i.e. given an almost infinite
 498 supply of computational resources, as one hones in closer and closer to the
 499 critical Reynolds number, a “tug of war” will be observed between the surface
 500 tension force trying to pull the bubble together versus the wall driven shear
 501 stress trying to pull the bubble apart.

502 4.4. Velocity field outside and inside the breaking bubble

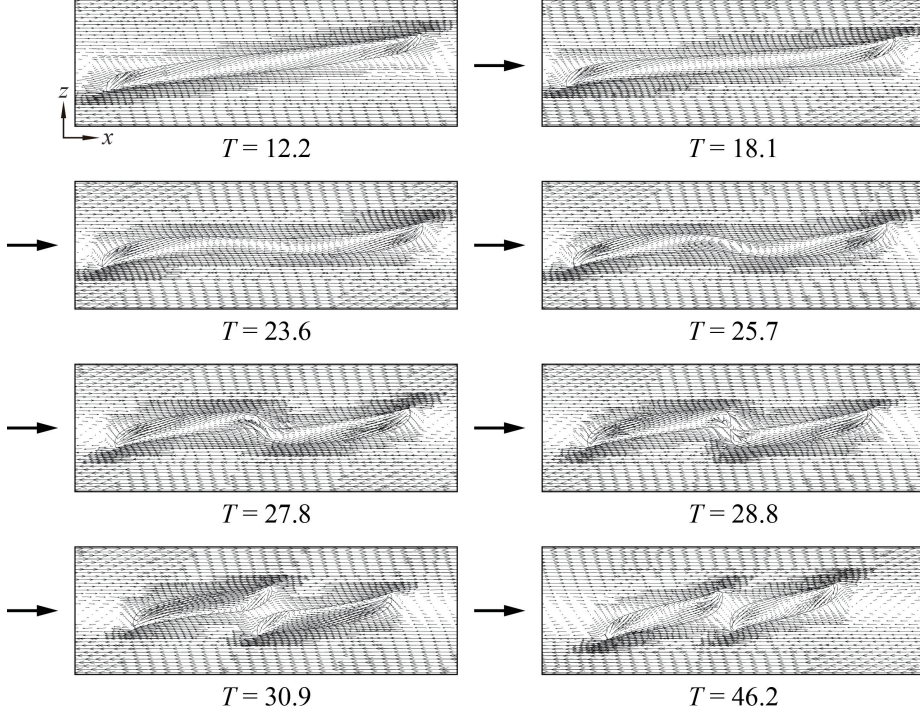


Figure 9: Fluid velocity field outside and inside the breaking bubble in shear flow at the condition $Ca = 0.3$ and $Re = 93$. The “bubble” critical Reynolds number corresponding to $Ca = 0.3$ is $92 < Re_c < 93$. ($\lambda = 1.2 \times 10^{-3}$, $\eta < 1.0 \times 10^{-3}$)

503 In this section, we consider the fluid flow velocity field outside and inside the
 504 bubble during the shear-induced breakup process. Detailed velocity fields of the
 505 deforming and breaking drop have already been presented in some references
 506 (Li et al. [22], Renardy and Cristini [32]). The velocity fields for the drop and
 507 the bubble will be influenced by the behavior of the breakup process, so the
 508 velocity fields for the drop and the bubble are not similar. Figure 9 shows the
 509 velocity fields outside and inside the bubble at cross-sectional slices in the xz
 510 plane for a flow condition of $Ca = 0.3$ and $Re = 93$. Regions around the bubble
 511 where there is a higher density of velocity vectors correspond to the level-1 grid
 512 portion of the AMR structure. The simulation results show that the velocity
 513 field inside the bubble is particularly distinct from the surrounding flow field
 514 in the exterior of the bubble. The cross-sections at $T = 12.2$ and $T = 18.1$,
 515 taken during the elongation phase, show how shear forces at the lower and
 516 upper halves of the bubble act along the bottom and top surfaces, respectively,
 517 to deform the interface. Near the left and right edges of the bubble, inward
 518 interior flows (that point toward the bubble center) begin to develop. Strong
 519 shearing forces in the exterior near the bottom-left-end and top-right-end of

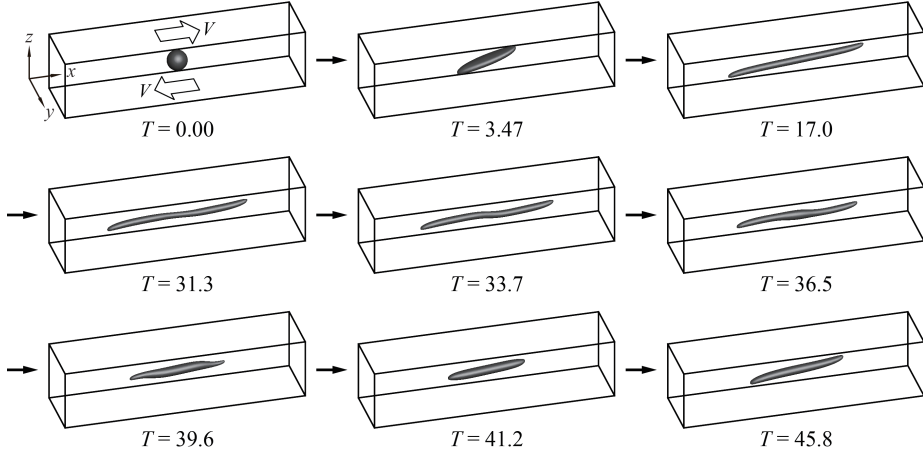


Figure 10: Time evolution of bubble deformation in shear flow at the condition of $Ca = 0.8$ and $Re = 42$. The “bubble” critical Reynolds number corresponding to $Ca = 0.8$ is $42 < Re_c < 43$. ($\lambda = 1.2 \times 10^{-3}$, $\eta < 1.0 \times 10^{-3}$)

the bubble interact with the interior flow field through the boundary to create cusped shapes at the bottom-left and top-right ends of the bubble while the interface is laterally elongated in the x -direction. During the shrinking process, which occurs for $23.6 \leq T \leq 27.8$, inward flows within the bubble extend over a wider region and are no longer localized near the bubble edges. Then, we observe that circulating flows form at the thread-bridge part of the doglegged bubble shape over the time interval [25.7, 27.8]. During the breakup process ($T \sim 28.8$), higher-intensity inward flows are formed inside the bubble, near the pinch off region, that are naturally larger than the surrounding interior flows and which are inextricably associated with the bubble migration illustrated in Figs. 6 and 7. As time proceeds further ($T = 46.2$), distinct inward flows are formed inside the daughter bubbles; the bubbles then begin their migration toward the side walls. Considering the left daughter bubble, for example, we see that the mechanism responsible for this movement results from larger shear forces acting on the bottom-left end than those in the top-left end.

4.5. Effect of surface tension on bubble deformation and breakup

In previous sections, we considered numerical simulations of bubble deformation and breakup with a capillary number $Ca = 0.3$. Here, we examine similar bubble dynamics with $Ca = 0.8$ and we also investigate the effect of interfacial tension on bubble deformation and breakup. Using $Ca = 0.8$ for both cases, Figures 10 and 11 present the time evolution of shear-induced bubble deformation and breakup with $Re = 42$ and $Re = 43$, respectively. We note that the bubble critical Reynolds number is around $Re_c \approx 43$, whereas $Re_c \approx 0$ for the corresponding case of the drop with $\lambda = \eta = 1$ (see e.g. Li et al. [22]). Note that Re_c for $Ca = 0.8$ is smaller than that for the condition of $Ca = 0.3$.

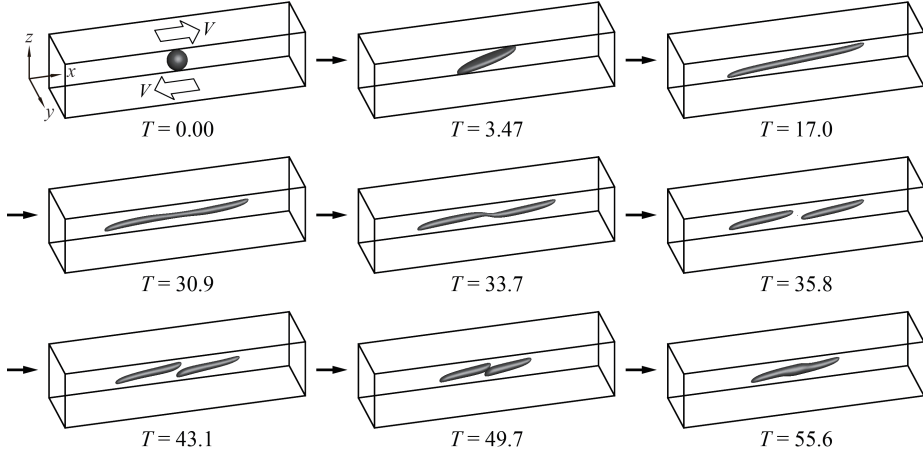


Figure 11: Time evolution of bubble deformation in shear flow at the condition of $Ca = 0.8$ and $Re = 43$. The “bubble” critical Reynolds number corresponding to $Ca = 0.8$ is $42 < Re_c < 43$. ($\lambda = 1.2 \times 10^{-3}$, $\eta < 1.0 \times 10^{-3}$)

since the bubble at $Ca = 0.8$ is more elastic due to the weaker effect of surface tension in this case. The results shown in Figs. 10 and 11 indicate that the bubble deformation and breakup process for the condition of $Ca = 0.8$ is analogous to that for $Ca = 0.3$. For the case of bubble deformation without breakup (Fig. 10), the bubble initially assumes a long elongated shape along the x -direction at around $T = 17.0$. The bubble then enters a compression stage over the time interval $[31.3, 41.2]$ and subsequently starts to elongate again at $T = 45.8$. On the other hand, for the case of bubble breakup (Fig. 11), an initial elongation phase is followed by a doglegged shape formation at $T = 33.7$. After that, the bubble ruptures from the thread-bridge part of the doglegged shape and two daughter bubbles are produced ($T = 35.8$). The two daughter bubbles formed after breakup move to the central area ($T = 49.7$) as in the case of $Ca = 0.8$ and $Re = 93$, but the two bubbles eventually coalesce in a region approximately centered in the computational domain ($T = 55.6$). We note that in a real experimental setting, bubbles may coalesce after breaking up due to slight deviations of flow conditions and states. Although the process of bubble deformation and breakup for flow conditions with $Ca = 0.3$ and $Ca = 0.8$ are similar, a pronounced difference is that the bubble for $Ca = 0.8$ is more elongated and slender than that for $Ca = 0.3$ due to the smaller effect of surface tension for $Ca = 0.8$.

Table 4 lists, for representative Ca values, the corresponding critical Reynolds number, Re_c , for shear-induced bubble breakup. The data in Table 4 corresponds to $\lambda = 1.2 \times 10^{-3}$, $\eta < 1.0 \times 10^{-3}$, $0.3 < Ca < 1$, and the initial/boundary conditions are given by (1). The results in Table 4 indicate that sufficiently large shear forces are required for bubble breakup even for large capillary numbers. In Figure 12 we plot the smooth interpolant of the data given in Table 4 and

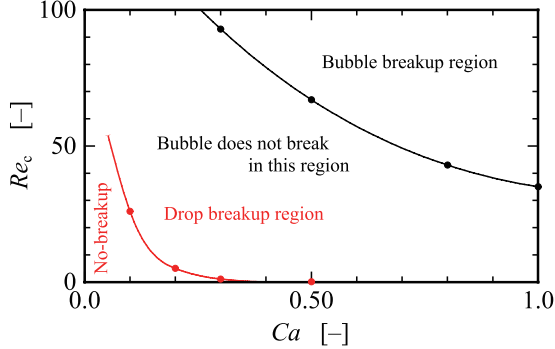


Figure 12: A plot of the critical Reynolds number versus capillary number for the data listed in Table 4. $\lambda = 1.2 \times 10^{-3}$, $\eta < 1.0 \times 10^{-3}$, $0.3 < Ca < 1$, and the initial/boundary conditions are given by (1). Given a new data point, (Ca, Re) , one can reliably predict whether the given (Ca, Re) pair will result in shear induced bubble break-up or not. Note, for the “Drop delineation curve,” $\lambda = \eta = 1$.

make the hypothesis that given a new data point, (Ca, Re) , shear induced bubble break up will occur if the point (Ca, Re) is above the given critical curve, and the bubble will not break if the (Ca, Re) pair is below the critical curve. For comparison, a critical curve for the drop with $\lambda = \eta = 1$ is also indicated in Fig. 12. The inclusion of breakup and no-breakup critical curves, for both the drop and the bubble, will facilitate future identification of Re_c numbers—and thus a more complete general critical curve—for a wide range of high Ca numbers.

Table 4: Shear-induced bubble breakup for various flow conditions described in terms of column pairs of critical Reynolds numbers and corresponding capillary numbers. ($\lambda = 1.2 \times 10^{-3}$, $\eta < 1.0 \times 10^{-3}$)

Capillary number Ca	0.3	0.5	0.8	1.0
Critical Reynolds number Re_c	93	67	43	35

5. Conclusions

The bubble deformation and breakup process in simple linear shear flow liquid was explored numerically using the CLSVOF computational method. In this study, the critical Reynolds number Re_c , at which bubble breakup first occurs, was determined for several flow conditions, and the differences between bubble deformation and breakup were compared with the well-known analogous process of drop deformation and breakup.

Numerical results revealed significant differences between bubble deformation and breakup and the corresponding drop dynamics. For case of bubble, it was discovered that much stronger shear flows are necessary to induce interface breakup compared with a drop immersed in a similar flow field. That

590 is, a much larger Reynolds number flow is required in order to induce bubble
 591 breakup. The behavior of bubble breakup was very similar through the Ca
 592 number range considered in our computations: the bubble underwent a simi-
 593 lar breakup mechanism in which rupture occurred at a thread-bridge part that
 594 followed a doglegged shape formation stage. In bubble deformation without
 595 breakup, near Re_c , the bubble did not maintain a stable deformed shape, in
 596 contrast to drop deformation near the critical Reynolds number. The bubble
 597 exhibited pronounced underdamped behavior: the bubble oscillated between
 598 elongating and shrinking motions for non-rupturing flow conditions. **At the**
 599 **same time, bubble deformation under smaller Re conditions ($< Re_c$) becomes**
 600 **in a stable state.** We attribute the large differences in morphology for the
 601 bubble undergoing breakup, compared with the drop, to the density and viscos-
 602 ity ratio. The density and viscosity ratio remarkably impacts on bubble/drop
 603 deformation and breakup. The bubble deformation and breakup is subject to a
 604 synergistic coupling of the density and viscosity ratio, and whose effect will be
 605 examined separately in future work.

606 References

- 607 [1] Amani, A., Balcázar, N., Castro, J., Oliva, A., 2019. Numerical study of droplet deformation in shear flow using a con-
 608 servative level-set method. *Chemical Engineering Science* 207,
 609 153–171. URL: <http://www.sciencedirect.com/science/article/pii/S0009250919305123>, doi:<https://doi.org/10.1016/j.ces.2019.06.014>.
- 613 [2] Bazhlekov, I.B., Anderson, P.D., Meijer, H.E., 2006. Numerical investi-
 614 gation of the effect of insoluble surfactants on drop deformation and
 615 breakup in simple shear flow. *Journal of Colloid and Interface Sci-
 616 ence* 298, 369 – 394. URL: <http://www.sciencedirect.com/science/article/pii/S0021979705012658>, doi:<http://dx.doi.org/10.1016/j.jcis.2005.12.017>.
- 619 [3] Bento, D., Rodrigues, R.O., Faustino, V., Pinho, D., Fernandes, C.S.,
 620 Pereira, A.I., Garcia, V., Miranda, J.M., Lima, R., 2018. Deforma-
 621 tion of red blood cells, air bubbles, and droplets in microfluidic devices:
 622 Flow visualizations and measurements. *Micromachines* 9, 151. URL:
 623 <https://www.mdpi.com/2072-666X/9/4/151>, doi:10.3390/mi9040151.
- 624 [4] Chu, P., Finch, J., Bournival, G., Ata, S., Hamlett, C., Pugh, R.J.,
 625 2019. A review of bubble break-up. *Advances in Colloid and In-
 626 terface Science* 270, 108–122. URL: <https://www.sciencedirect.com/science/article/pii/S0001868619300211>, doi:<https://doi.org/10.1016/j.cis.2019.05.010>.
- 629 [5] Cristini, V., Bławzdziewicz, J., Loewenberg, M., 2001. An adap-
 630 tive mesh algorithm for evolving surfaces: simulations of drop breakup

- 631 and coalescence. Journal of Computational Physics 168, 445 –
 632 463. URL: <http://www.sciencedirect.com/science/article/pii/S0021999101967130>, doi:<http://dx.doi.org/10.1006/jcph.2001.6713>.
- 633
- 634 [6] Cristini, V., Guido, S., Alfani, A., Bławzdziewicz, J., Loewenberg, M.,
 635 2003. Drop breakup and fragment size distribution in shear flow. Journal
 636 of Rheology 47, 1283–1298. URL: <http://scitation.aip.org/content/sor/journal/jor2/47/5/10.1122/1.1603240>, doi:<http://dx.doi.org/10.1122/1.1603240>.
- 637
- 638
- 639 [7] Croce, R., Griebel, M., Schweitzer, M.A., 2010. Numerical simulation of
 640 bubble and droplet deformation by a level set approach with surface tension
 641 in three dimensions. International Journal for Numerical Methods in Fluids
 642 62, 963–993. URL: <http://dx.doi.org/10.1002/fld.2051>, doi:10.1002/fld.2051.
- 643
- 644 [8] Drenckhan, W., Saint-Jalmes, A., 2015. The science of foaming. Advances
 645 in Colloid and Interface Science 222, 228–259. URL: <https://www.sciencedirect.com/science/article/pii/S0001868615000603>,
 646 doi:<https://doi.org/10.1016/j.cis.2015.04.001>. reinhard Miller,
 647 Honorary Issue.
- 648
- 649 [9] Ervin, E., Tryggvason, G., 1997. The rise of bubbles in a vertical shear
 650 flow. Journal of Fluids Engineering 119(2), 443–449.
- 651
- 652 [10] Hernandez, F.H., Rangel, R.H., 2017. Breakup of drops in simple
 653 shear flows with high-confinement geometry. Computers & Fluids 146,
 654 23 – 41. URL: <http://www.sciencedirect.com/science/article/pii/S0045793017300038>, doi:<https://doi.org/10.1016/j.compfluid.2017.01.001>.
- 655
- 656 [11] Hirt, C., Nichols, B., 1981. Volume of fluid (vof) method
 657 for the dynamics of free boundaries. Journal of Computational
 658 Physics 39, 201 – 225. URL: <http://www.sciencedirect.com/science/article/pii/0021999181901455>, doi:[http://dx.doi.org/10.1016/0021-9991\(81\)90145-5](http://dx.doi.org/10.1016/0021-9991(81)90145-5).
- 659
- 660
- 661 [12] Inamuro, T., 2006. Lattice boltzmann methods for viscous fluid flows and
 662 for two-phase fluid flows. Fluid Dynamics Research 38, 641. URL: <http://stacks.iop.org/1873-7005/38/i=9/a=A04>.
- 663
- 664 [13] Inamuro, T., Tomita, R., Ogino, F., 2003. Lattice boltzmann simulations
 665 of drop deformation and breakup in simple shear flows. International Journal of Modern Physics B 17, 21–26. URL: <http://www.worldscientific.com/doi/abs/10.1142/S0217979203017035>, doi:10.1142/S0217979203017035.
- 666
- 667
- 668
- 669 [14] Ioannou, N., Liu, H., Zhang, Y., 2016. Droplet dynamics
 670 in confinement. Journal of Computational Science 17, 463 –
- 671

- 671 474. URL: <http://www.sciencedirect.com/science/article/pii/S1877750316300308>, doi:<https://doi.org/10.1016/j.jocs.2016.03.009>. discrete Simulation of Fluid Dynamics 2015.
- 674 [15] Janssen, P., Anderson, P., 2008. A boundary-integral model for
675 drop deformation between two parallel plates with non-unit viscosity
676 ratio drops. Journal of Computational Physics 227, 8807–
677 8819. URL: <http://www.sciencedirect.com/science/article/pii/S002199910800346X>, doi:<http://dx.doi.org/10.1016/j.jcp.2008.06.027>.
- 680 [16] Janssen, P.J.A., Anderson, P.D., 2007. Boundary-integral method
681 for drop deformation between parallel plates. Physics of Fluids
682 19. URL: <http://scitation.aip.org/content/aip/journal/pof2/19/4/10.1063/1.2715621>, doi:<http://dx.doi.org/10.1063/1.2715621>.
- 684 [17] Kang, M., Fedkiw, R.P., Liu, X.D., 2000. A boundary condition capturing
685 method for multiphase incompressible flow. Journal of scientific computing
686 15, 323–360.
- 687 [18] Khismatullin, D.B., Renardy, Y., Cristini, V., 2003. Inertia-induced
688 breakup of highly viscous drops subjected to simple shear. Physics of Fluids
689 15, 1351–1354. doi:<http://dx.doi.org/10.1063/1.1564825>".
- 690 [19] Komrakova, A., Shardt, O., Eskin, D., Derksen, J., 2014. Lattice
691 boltzmann simulations of drop deformation and breakup in shear flow.
692 International Journal of Multiphase Flow 59, 24 – 43. URL: <http://www.sciencedirect.com/science/article/pii/S0301932213001547>,
693 doi:<http://dx.doi.org/10.1016/j.ijmultiphaseflow.2013.10.009>.
- 695 [20] Komrakova, A., Shardt, O., Eskin, D., Derksen, J., 2015. Effects
696 of dispersed phase viscosity on drop deformation and breakup
697 in inertial shear flow. Chemical Engineering Science 126, 150 –
698 159. URL: <http://www.sciencedirect.com/science/article/pii/S000925091400726X>, doi:<http://dx.doi.org/10.1016/j.ces.2014.12.012>.
- 701 [21] Legendre, D., Magnaudet, J., 1998. The lift force on a spherical bubble in
702 a viscous linear shear flow. Journal of Fluid Mechanics 368, 81–126.
- 703 [22] Li, J., Renardy, Y., Renardy, M., 2000. Numerical simulation of
704 breakup of a viscous drop in simple shear flow through a volume-of-fluid
705 method. Physics of Fluids 12, 269–282. URL: <http://scitation.aip.org/content/aip/journal/pof2/12/2/10.1063/1.870305>, doi:<http://dx.doi.org/10.1063/1.870305>.
- 708 [23] Müller-Fischer, N., Tobler, P., Dressler, M., Fischer, P., Windhab, E.J.,
709 2008. Single bubble deformation and breakup in simple shear flow. Experiments
710 in fluids 45, 917–926.

- 711 [24] Ohta, M., Akama, Y., Yoshida, Y., Sussman, M., 2014. Influence of the
 712 viscosity ratio on drop dynamics and breakup for a drop rising in an im-
 713 miscible low-viscosity liquid. *Journal of Fluid Mechanics* 752, 383–409.
 714 doi:10.1017/jfm.2014.339.
- 715 [25] Ohta, M., Furukawa, T., Yoshida, Y., Sussman, M., 2019. A
 716 three-dimensional numerical study on the dynamics and deformation
 717 of a bubble rising in a hybrid carreau and fene-cr modeled poly-
 718 mERIC liquid. *Journal of Non-Newtonian Fluid Mechanics* 265, 66–
 719 78. URL: <https://www.sciencedirect.com/science/article/pii/S0377025718301952>, doi:<https://doi.org/10.1016/j.jnnfm.2018.12.012>.
- 722 [26] Ohta, M., Kikuchi, D., Yoshida, Y., Sussman, M., 2011. Robust numeri-
 723 cal analysis of the dynamic bubble formation process in a viscous liquid.
 724 *International Journal of Multiphase Flow* 37, 1059–1071.
- 725 [27] Ohta, M., Sussman, M., 2012. The buoyancy-driven mo-
 726 tion of a single skirted bubble or drop rising through
 727 a viscous liquid. *Physics of Fluids* 24, 112101. URL:
 728 <https://doi.org/10.1063/1.4765669>, doi:10.1063/1.4765669,
 729 arXiv:https://pubs.aip.org/aip/pof/article-pdf/doi/10.1063/1.4765669/14128560/112101_1_o
- 730 [28] Rallison, J.M., 1984. The deformation of small viscous drops
 731 and bubbles in shear flows. *Annual Review of Fluid Mechan-
 732 ics* 16, 45–66. URL: <http://dx.doi.org/10.1146/annurev.fl.16.010184.000401>,
 733 doi:10.1146/annurev.fl.16.010184.000401,
 734 arXiv:<http://dx.doi.org/10.1146/annurev.fl.16.010184.000401>.
- 735 [29] Renardy, Y., 2006. Numerical simulation of a drop undergoing large am-
 736 plitude oscillatory shear. *Rheologica acta* 45, 223–227.
- 737 [30] Renardy, Y., 2007. The effects of confinement and inertia on the production
 738 of droplets. *Rheologica Acta* 46, 521–529. URL: <http://dx.doi.org/10.1007/s00397-006-0150-y>, doi:10.1007/s00397-006-0150-y.
- 740 [31] Renardy, Y., 2008. Effect of startup conditions on drop breakup under
 741 shear with inertia. *International Journal of Multiphase Flow*
 742 34, 1185 – 1189. URL: <https://www.sciencedirect.com/science/article/pii/S030193220800089X>, doi:<https://doi.org/10.1016/j.ijmultiphaseflow.2008.04.004>.
- 745 [32] Renardy, Y., Cristini, V., 2001a. Effect of inertia on drop breakup under
 746 shear. *Physics of Fluids* 13, 7–13. URL: <http://scitation.aip.org/content/aip/journal/pof2/13/1/10.1063/1.1331321>, doi:<https://doi.org/10.1063/1.1331321>.
- 749 [33] Renardy, Y., Cristini, V., Li, J., 2002. Drop fragment distributions un-
 750 der shear with inertia. *International Journal of Multiphase Flow* 28, 1125

- 751 – 1147. URL: <http://www.sciencedirect.com/science/article/pii/S0301932202000228>, doi:[http://dx.doi.org/10.1016/S0301-9322\(02\)00022-8](http://dx.doi.org/10.1016/S0301-9322(02)00022-8).
- 754 [34] Renardy, Y.Y., Cristini, V., 2001b. Scalings for fragments produced
 755 from drop breakup in shear flow with inertia. Physics of Fluids 13,
 756 2161–2164. URL: <https://doi.org/10.1063/1.1384469>, doi:10.1063/
 757 1.1384469, arXiv:<https://doi.org/10.1063/1.1384469>.
- 758 [35] Rust, A., Manga, M., 2002. Bubble shapes and orientations in low re
 759 simple shear flow. Journal of Colloid and Interface Science 249, 476–
 760 480. URL: <https://www.sciencedirect.com/science/article/pii/S0021979702982925>, doi:<https://doi.org/10.1006/jcis.2002.8292>.
- 762 [36] Stone, H.A., 1994. Dynamics of drop deformation and breakup
 763 in viscous fluids. Annual Review of Fluid Mechanics 26,
 764 65–102. URL: <http://dx.doi.org/10.1146/annurev.fl.26.010194.000433>,
 765 doi:10.1146/annurev.fl.26.010194.000433,
 766 arXiv:<http://dx.doi.org/10.1146/annurev.fl.26.010194.000433>.
- 767 [37] Sussman, M., 2003. A second order coupled level set and volume-
 768 of-fluid method for computing growth and collapse of vapor bubbles.
 769 Journal of Computational Physics 187, 110–136. URL: <https://www.sciencedirect.com/science/article/pii/S0021999103000871>,
 770 doi:[https://doi.org/10.1016/S0021-9991\(03\)00087-1](https://doi.org/10.1016/S0021-9991(03)00087-1).
- 772 [38] Sussman, M., Almgren, A.S., Bell, J.B., Colella, P., Howell, L.H.,
 773 Welcome, M.L., 1999. An adaptive level set approach for incom-
 774 pressible two-phase flows. Journal of Computational Physics 148, 81
 775 – 124. URL: <http://www.sciencedirect.com/science/article/pii/S002199919896106X>, doi:<https://doi.org/10.1006/jcph.1998.6106>.
- 777 [39] Sussman, M., Puckett, E.G., 2000. A coupled level set and
 778 volume-of-fluid method for computing 3d and axisymmetric incompress-
 779 ible two-phase flows. Journal of Computational Physics 162, 301–
 780 337. URL: <http://www.sciencedirect.com/science/article/pii/S0021999100965379>, doi:<http://dx.doi.org/10.1006/jcph.2000.6537>.
- 782 [40] Sussman, M., Smereka, P., Osher, S., 1994. A level set ap-
 783 proach for computing solutions to incompressible two-phase flow.
 784 Journal of Computational Physics 114, 146 – 159. URL: <http://www.sciencedirect.com/science/article/pii/S0021999184711557>,
 785 doi:<http://dx.doi.org/10.1006/jcph.1994.1155>.
- 787 [41] Sussman, M., Smith, K., Hussaini, M., Ohta, M., Zhi-Wei, R., 2007. A
 788 sharp interface method for incompressible two-phase flows. Journal of Com-
 789 putational Physics 221, 469–505. URL: <https://www.sciencedirect.com/science/article/pii/S0021999106002981>, doi:<https://doi.org/10.1016/j.jcp.2006.06.020>.

- 792 [42] Tanguy, S., Ménard, T., Berlemont, A., 2007. A level set method for
793 vaporizing two-phase flows. *Journal of Computational Physics* 221, 837–
794 853.
- 795 [43] Taylor, G.I., 1932. The viscosity of a fluid containing small drops of another
796 fluid. *Proceedings of the Royal Society of London A: Mathematical, Physi-*
797 *cal and Engineering Sciences* 138, 41–48. doi:10.1098/rspa.1932.0169.
- 798 [44] Taylor, G.I., 1934. The formation of emulsions in definable fields of flow.
799 *Proceedings of the Royal Society of London A: Mathematical, Physical and*
800 *Engineering Sciences* 146, 501–523. doi:10.1098/rspa.1934.0169.
- 801 [45] Unverdi, S.O., Tryggvason, G., 1992. A front-tracking method
802 for viscous, incompressible, multi-fluid flows. *Journal of Computa-*
803 *tional Physics* 100, 25 – 37. URL: <http://www.sciencedirect.com/science/article/pii/002199919290307K>, doi:[http://dx.doi.org/10.1016/0021-9991\(92\)90307-K](http://dx.doi.org/10.1016/0021-9991(92)90307-K).
- 806 [46] Wang, Z., Shi, D., Zhang, A., 2015. Three-dimensional lattice boltz-
807 man simulation of bubble behavior in a flap-induced shear flow. *Com-*
808 *puters & Fluids* 123, 44 – 53. URL: <http://www.sciencedirect.com/science/article/pii/S0045793015003199>, doi:<https://doi.org/10.1016/j.compfluid.2015.09.007>.
- 811 [47] Wei, Y.K., Qian, Y., Xu, H., 2012. Lattice boltzmann simulations
812 of single bubble deformation and breakup in a shear flow. *The Jour-*
813 *nal of Computational Multiphase Flows* 4, 111–117. URL: <https://doi.org/10.1260/1757-482X.4.1.111>, doi:10.1260/1757-482X.4.1.111,
815 arXiv:<https://doi.org/10.1260/1757-482X.4.1.111>.
- 816 [48] Zhang, J., Miksis, M.J., Bankoff, S.G., 2006. Nonlinear dynamics of
817 a two-dimensional viscous drop under shear flow. *Physics of Fluids*
818 18. URL: <http://scitation.aip.org/content/aip/journal/pof2/18/7/10.1063/1.2222336>, doi:<http://dx.doi.org/10.1063/1.2222336>.
- 820 [49] Zhang, J., Ni, M.J., Magnaudet, J., 2021a. Three-dimensional dynamics
821 of a pair of deformable bubbles rising initially in line. part 1. moderately
822 inertial regimes. *Journal of Fluid Mechanics* 920, A16.
- 823 [50] Zhang, J., Ni, M.J., Magnaudet, J., 2022. Three-dimensional dynamics of
824 a pair of deformable bubbles rising initially in line. part 2. highly inertial
825 regimes. *Journal of Fluid Mechanics* 943, A10.
- 826 [51] Zhang, J., Shu, S., Guan, X., Yang, N., 2021b. Regime map-
827 ping of multiple breakup of droplets in shear flow by phase-field
828 lattice boltzmann simulation. *Chemical Engineering Science* 240,
829 116673. URL: <https://www.sciencedirect.com/science/article/pii/S0009250921002384>, doi:<https://doi.org/10.1016/j.ces.2021.116673>.